Applied Catalysis B: Environmental 254 (2019) 560–568

Contents lists available at ScienceDirect

Applied Catalysis B: Environmental

journal homepage: www.elsevier.com/locate/apcatb

Metal-acid interfaces enveloped in zeolite crystals for cascade biomass hydrodeoxygenation

Zhu Jin[b,1], Xianfeng Yi[c,1], Liang Wang[a,**], Shaodan Xu[d], Chengtao Wang[b], Qinming Wu[b], Lingxiang Wang[b], Anmin Zheng[c,**], Feng-Shou Xiao[a,b,*]

[a] Key Lab of Biomass Chemical Engineering of Ministry of Education, College of Chemical and Biological Engineering, Zhejiang University, Hangzhou, 310027, China
[b] Key Lab of Applied Chemistry of Zhejiang Province, Department of Chemistry, Zhejiang University, Hangzhou, 310028, China
[c] National Center for Magnetic Resonance in Wuhan, Key Laboratory of Magnetic Resonance in Biological Systems, State Key Laboratory of Magnetic Resonance and Atomic and Molecular Physics and Mathematics, Wuhan Institute of Physics and Mathematics, Chinese Academy of Sciences, Wuhan, 430071, China
[d] College of Materials and Environmental Engineering, Hangzhou Dianzi University, Hangzhou, 310018, China

ARTICLE INFO

Keywords:
Zeolite
Core-shell structure
Bifunctional catalyst
Biomass

ABSTRACT

A wide scope of catalytic reactions require combined steps to realize a one-pot transformation over multifunctional catalysts, but their synergism is still insufficient. Here, it is demonstrated a methodology for synergizing different active sites by enveloping the sulfonic acid group and Pd nanoparticles within FAU zeolite crystals (Pd^SO$_3$H@Y). This approach realizes the geometrically closest Pd nanoparticles with acid sites immobilized by the zeolite framework, forming metal-acid interfaces to strengthen the cascade catalysis. In the model reaction of hydrodeoxygenation of furfural, a process for upgrading the biomass-derived oxygenate, the Pd^SO$_3$H@Y exhibits methyl furan selectivity for 99.3% with complete conversion of furfural, which steadily outperforms catalytic properties of the generally supported catalysts. More importantly, the rigid zeolite crystals stabilize the metal-acid interfaces, achieving stable catalytic performances in the continuously recycle tests.

1. Introduction

In synthetic chemistry, the reactions with multiple steps are necessary to produce desirable compounds, where various catalysts are employed for the corresponding steps [1–9]. In these cases, the tedious separation and purification of intermediate products are necessary, which is time-consuming and energy-cost. To overcome these issues, it is suggested to realize a "one-pot" transformation from combination of several steps over multifunctional catalysts in modern chemistry [10–14]. A typical process is the transformation of biomass-derived intermediates into valuable products and alternative fuels, which act as processes for the renewable energy utilization and environmental protection. Such reaction usually requires late-transition metals and acids for the catalytic hydrodeoxygenation (HDO) [6,15–22]. In this process involving several individual reactions, the synergism of metal and acid sites is crucial for catalytic performances. The extensively used catalysts are liquid acids (e.g. HCl, H_2SO_4) and supported metal nanoparticles [15,23–25]. However, the liquid acids are chemically corrosive, which strongly limit the practical applications. For a mixture of acidic catalysts and supported metal nanoparticles in the cascade catalysis, it is remarkably hindered by the diffusion of reaction intermediates due to the spatially separated metal nanoparticles and acid sites. To shorten the metal-acid distance, it is developed to functionalize acidic ionic liquids on silica for supporting metal nanoparticles or assemble acidic molecules on the metal nanoparticle surface [19,26], which significantly enhances the metal-acid synergism by constructing the metal-acid interfaces. However, the durability of these catalysts for long-period reaction is not enough because the motion of metal/acid on the catalyst surface would break the metal-acid interfaces. In addition, the deactivation also occurs from the metal and acid leaching during the reaction. Despite growing number of bifunctional metal-acid catalysts, the ideal catalysts with high activity, selectivity, and excellent durability in the cascade catalysis for potential application is still challenging yet.

Herein, we report how the synergism of metal nanoparticles and acid sites can be strengthened to overcome the aforementioned

* Corresponding author at: Key Lab of Biomass Chemical Engineering of Ministry of Education, College of Chemical and Biological Engineering, Zhejiang University, Hangzhou, 310027, China.
** Corresponding authors.
E-mail addresses: liangwang@zju.edu.cn (L. Wang), zhenganm@wipm.ac.cn (A. Zheng), fsxiao@zju.edu.cn (F.-S. Xiao).
[1] Z. Jin and X. Yi contributed equally.

https://doi.org/10.1016/j.apcatb.2019.05.022
Received 17 March 2019; Received in revised form 1 May 2019; Accepted 5 May 2019
Available online 08 May 2019
0926-3373/ © 2019 Published by Elsevier B.V.

limitations. Considering Pd nanoparticles and sulfonic acids are widely investigated in HDO, we have enveloped them within the FAU zeolite crystals to obtain zeolite containing bifunctional metal and Brønsted acid sites (Pd^SO_3H@Y), where the geometrically closest metal nanoparticles with acid centers are formed, resulting in the formation of catalytically active Pd-acid interfaces. Synchronously, the zeolite micropores benefit the diffusion of reactant/product molecules to access to the Pd-acid species. These features provide a good opportunity for accelerating the bifunctional catalysis, significantly improving the catalytic activities and selectivities towards the HDO of furfural, a biomass-derived platform oxygenate. More importantly, the rigid zeolite framework efficiently immobilizes the Pd nanoparticles and sulfonic acid groups to stabilize the Pd-acid interfaces, giving excellent durability in the recycling tests.

2. Experimental

2.1. Synthesis

Synthesis of -SH stabilized Pd colloid and Pd^SH@SiO_2. In the synthesis of Pd colloid, 1.16 g of Na_2PdCl_4 aqueous solution (8.6 mg/g, 10 mg of Pd) was added into 100 mL of acetone under stirring at 0 °C, followed by the addition of 3-mercaptopropyl(dimethoxy) methylsilane (0.017, 0.085, and 0.170 g for the samples with S/Pd at 1, 5, and 10, respectively). Then 10 mL of methanol was added and stirred for another 6 h to obtain the colloid.

The Pd^SH@SiO_2 was obtained by the controllable hydrolysis of the aforementioned colloid solution. 80 mL of ethanol and 6 mL of ammonia aqueous solution (25–28%) were added into the as-prepared Pd colloid. After stirring at room temperature for 0.5 h, the TEOS (3.453, 3.375, and 3.277 g for the samples with S/Pd at 1, 5, and 10, respectively) was added and stirred for another 12 h. Then the mixture was distilled under vacuum at 60 °C to remove the solvent and dried at 100 °C for 12 h to obtain the Pd^SH@SiO_2 samples.

Synthesis of Pd^SH@Y. The zeolite samples were synthesized via the crystallization system with a composition at 8.0 SiO_2/1.0 Al_2O_3/4.14 Na_2O/133 H_2O/0.036 Pd /0.036-0.36 SH. 0.415 g of $NaAlO_2$ and 0.635 g of NaOH were dissolved in 6.05 g of water, following by the addition of the as-prepared Pd^SH@SiO_2 sample. After stirring at room temperature for 12 h, the gel was transferred to a Teflon-lined stainless steel autoclave and hydrothermally treated at 100 °C for 24 h. After filtering and washing with ethanol and distilled water for three times and drying at 60 °C for 6 h, the Pd^SH@Y sample was obtained.

Synthesis of Pd^SO_3H@Y. 1 g of Pd^SH@Y sample was stirred within the 50 mL of acetic acid aqueous solution (1 M) for 1 h at 70 °C for exchanging the Na^+ cations in to H^+ in the zeolite framework, then the solid sample was separated from the liquor and redispersed within the fresh acetic acid aqueous solution (0.5 M). The aforementioned ion-exchange treatment was performed by four times for the maximized ion exchange. Then, 1 g of the obtain solid sample after ion exchange was dispersed within 20 mL of water at 40 °C under stirring, followed by adding 1.3 g of H_2O_2 (30%, dropwise addition in 1 h) and stirring for another 6 h to oxidize the -SH groups into -SO_3H. After filtrating, washing with water, drying at 60 °C for 12 h, and reducing with gaseous H_2 at 220 °C for 2 h, the Pd^SO_3H@Y samples were finally obtained. The Pd^SO_3H@Y samples with different S concentrations were synthesized in the same procedures except using the different Pd^SH@SiO_2 precursors. The Pd loading in the final catalysts were analyzed to be 0.78–0.80 wt%.

Synthesis of Y-SO_3H. 1 g of as-synthesized Y zeolite was dried under vacuum at 150 °C, and then dispersed in 100 mL of anhydrous toluene. After ultrasonic treatment for 20 min, 1 g of 3-mercaptopropyl(dimethoxy) methylsilane was added into the mixture, stirring for 10 min at room temperature. Then the mixture was heated to 100 °C in an oil bath, and stirred for another 10 h. After filtrating, washing with a large amount of anhydrous toluene and ethanol to remove the unreacted 3-mercaptopropyl(dimethoxy) methylsilane, and drying at 100 °C for 4 h, the Y−SH was obtained. Then, 1 g of the obtain solid sample after ion exchange was dispersed within 20 mL of water at 40 °C under stirring, followed by adding 1.3 g of H_2O_2 (30%, dropwise addition in 1 h) and stirring for another 6 h to oxidize the -SH groups into -SO_3H to obtain the Y-SO_3H sample.

Synthesis of Pd/Y-SO_3H. The Pd nanoparticles were loaded via the conventional deposition method. 1 g of Y-SO_3H was mixed with 2 g of aqueous solution of Na_2PdCl_4 (Pd concentration at 4 mg/g) under ultrasonic treatment at 40 °C for 3 h, then the water was removed at 40 °C under grinding by hand. The Pd nanoparticles were formed by reduction with gaseous H_2 at 220 °C for 2 h. After washing with acetic acid aqueous solution (1 M) for 1 h at 70 °C, the Pd/Y-SO_3H sample with Pd loading at 0.78 wt% was finally obtained.

The procedures for the synthesis of Y zeolite, Pd/PVP colloid, Pd@SiO_2, and Pd@Y are presented in the Supporting Information.

2.2. Characterization

X-ray diffraction (XRD) data were collected on a Rigaku D/MAX 2550 diffractometer with Cu Kα (λ = 1.5418 Å). The amount of Pd elements was determined by inductively coupled plasma (ICP) analysis (Perkin-Elmer 3300DV). Nitrogen adsorption-desorption isotherms were measured using a Micromeritics ASAP2020 system. Transmission electronmicroscopy (TEM), scanning transmission electron microscopy (STEM), and energy dispersivespectrometer (EDS) were performed on a JEM-2100 F electron microscopy (JEOL, Japan) with an acceleration voltage of 200 kV. Thermogravimetric curves (TG) were performed on a SDT Q600 Simultaneous DSC-TGA in flowing air with heating rate of 10 °C/min. SEM experiments were performed with a Hitachi SU8010 electron microscopes. The $^1H \rightarrow ^{29}Si$ CP/MAS NMR experiment was performed on a Bruker Avance III 600 solid-state spectrometer equipped with a 4 mm double resonance MAS probe with a spinning rate of 10 kHz. The ^{13}C MAS NMR experiment was performed on a Bruker Avance III-600 solid-state spectrometer at 119.2 MHz, using a 4 mm double resonance MAS probe with a spinning rate of 6 kHz, 500 scans, and a recycle delay of 4 s. The FTIR spectra were recorded with a Bruker Vestor 22 FTIR spectrometer equipped with an MCT/A detector. In the pyridine-adsorption FTIR test, 50 mg of catalyst was fixed in the sample cell and pretreated at 200 °C for 1 h under vacuum, then the cell was reduced to 50 °C and the gaseous pyridine was introduced. After adsorption for 1 h, the samples was treated at 50 or 400 °C under vacuum for 1 h, and then the IR spectra were collected.

2.3. Catalytic tests

The hydrodeoxygenation was performed in a high-pressure autoclave with a magnetic stirrer (1200 rpm). In the hydrodeoxygenation of furfural, 1.0 mmol of furfural, 40 mg of catalyst, and 6 mL of methanol solvent were mixed in the reactor, followed by stirring for 10 min at room temperature. Then mixed gas of H_2 and Ar with molar ratio of H_2/Ar at 1 was introduced, and the reaction system was heated to a 130 °C (the temperature was measured with a thermometer in an oil bath, the hydrogen pressure in autoclave was recorded at reaction temperature). After the reaction, the product was taken out from the reaction system and analyzed by gas chromatography (GC-14C, Shimadzu, using a flame ionization detector) with a flexible quartz capillary column coated with OV-17 and FFAP using ethylbenzene or bromobenzene as internal standard (internal standard was added after reaction). The product selectivities were based on the amount of furan/tetrahydrofuran rings in the products. The HDO of phenol and cresol was performed with similar procedures except for using different feeds and reaction conditions. The selectivities in HDO of phenol and cresol were based on the amount of carbon atoms in the products. The recyclability of the catalyst was tested by separating it from the reaction system by centrifugation and washing with large quantity of ethanol/water and

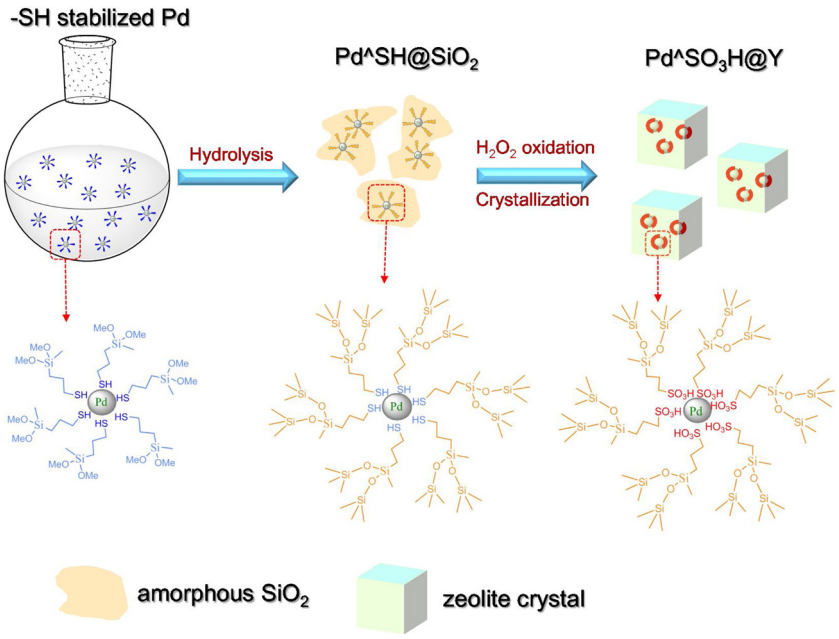

Scheme 1. Synthesis procedures of Pd^SO_3H@Y catalyst.

drying at 80 °C for 4 h.

3. Results and discussion

3.1. Synthesis and characterization

Scheme 1 represents procedures for preparing Pd^SO_3H@Y. The Pd^SO_3H@Y was derived from a 3-mercaptopropyl(dimethoxy)methylsilane coordinated with Pd nanoparticles. Such species were hydrolyzed to obtain amorphous silica capsulated Pd nanoparticles (Pd^SH@SiO_2), which was used as a partial silica source in the zeolite crystallization system with a composition at 8.0 SiO_2 /1.0 Al_2O_3 /4.14 Na_2O /133 H_2O /0.036 Pd /0.036-0.36 SH. After crystallization at 100 °C for 24 h, the Pd^SH@Y was obtained. By oxidation with hydrogen peroxide, the thiol group was transformed into sulfonic acid group. The concentration of the sulfonic acid enables to be adjusted by changing the amount of SH-containing silica in the starting gel. The final catalyst was denoted as Pd^SO_3H@Y-*x*, where the *x* is the molar ratio of sulfur to Pd in the synthetic precursors. For comparison, the Y zeolite enveloped Pd catalyst without sulfonic acid groups was synthesized from similar procedures except for the absence of organosilane in the precursors (Pd@Y); supported Pd and sulfonic acid catalyst was synthesized from loading Pd on the sulfonic acid functionalized Y zeolite (Pd/Y-SO_3H, molar ratio of sulfur to Pd at 5).

Fig. 1a shows XRD patterns of Pd^SO_3H@Y samples with different S/Pd ratios, exhibiting typical peaks assigning to FAU zeolite structure (Figs. S1 and S2). N_2 adsorption-desorption isotherms of the Pd^SO_3H@Y samples show type-I curves associated with characteristic microporous structure (Fig. 1b), confirming the successful formation of zeolite structure even with the existence of Pd nanoparticles and sulfonic acid groups (Table S1). Notably, the samples have high surface area at 700-839 cm^2/g and pore volume at 0.31-0.43 cm^3/g. Characterizations with scanning electron microscopy confirm the Pd^SO_3H@Y samples have high purity and crystallinity, exhibiting similar crystal diameters to those of conventional Y zeolite crystals (Fig. S2).

The functionalization of sulfuric acid groups were investigated by ^{29}Si and ^{13}C NMR spectroscopy. As shown in Fig. 1c, the Pd^SO_3H@Y-5 and Pd@Y (Figs. S3 and S4) exhibit similar ^{29}Si NMR signal at −90 ~ −120 ppm, which are assigned to the Si sites coordinated with Si and Al species in the framework. Compared with Pd@Y, the Pd^SO_3H@Y-5 has additional signals at −11 and −19 ppm, which is related to the Si coordinated to carbon species. The existence of SO_3H is further supported by the ^{13}C NMR spectrocopy, where the Pd^SO_3H@Y-5 gives strong signals at 15–33 ppm assigned to the carbon species on the organosilane groups (Fig. S5). In contrast, such signal is absent on the Pd@Y because of the lack of organic species [27]. Compared with Y zeolite, the Pd^SO_3H@Y-5 exhibited a series of additional peaks in the FTIR spectrum. The bands at 2948, 2876, and 1460 cm^{-1} are associated with the presence of $-CH_2-$ group. Appearance of the bands at 1272 and 965 cm^{-1} means the presence of Si-C and C–S species. The wides band at 1080 cm^{-1} are attributed to the signal of O = S=O species (Fig. S6a). These data confirm the successful functionalization of organic groups into the zeolite framework. In the TG analysis of the Pd^SO_3H@Y-5 (Fig. S6b), a significant weight loss before 200 °C is assigned to the loss of adsorbed water and other species on the sample. A slight weight loss centralized at 281 °C is due to the removal of organosilane species, confirming the organic groups are stable at desired reaciton temperature (< 200 °C).

The Pd nanoparticles are directly observed by a series of electronic microscopic characterizations. Fig. 2a-c show high-angle annular dark-field scanning transmission electron microscopic (HAADF-STEM) images of the Pd^SO_3H@Y-1, Pd^SO_3H@Y-5, and Pd^SO_3H@Y-10 samples. The Pd nanoparticles and zeolite matrix are distinguished from each other by the remarkably different brightness contrast in the HAADF-STEM images, where the Pd nanoparticles with relatively brighter contrast have uniform distribution with diameter at 2–8 nm in the zeolite with less brightness (Fig. S7). The evidence for identifying the location of Pd nanoparticles is achieved by the C–S tomographic-section transmission electronic microscopic characterization (TEM), where the zeolite crystals were pre-cut into slices for TEM characterization to avoid the influence the Pd nanoparticles on the external surface of zeolite crystals. The C–S tomographic-section STEM and TEM images of Pd^SO_3H@Y-5 give Pd nanoparticles dispersed in the region of zeolite crystals (Fig. 2d and e), confirming the Pd nanoparticles are indeed enveloped into the zeolite crystals. In contrast, the Pd/Y-SO_3H has only Pd nanoparticles on the outside of zeolite region (Figs. S8 and S9, Table S1).

Local environment of Pd nanoparticles within the zeolite crystals is investigated by the energy dispersive spectroscopy (EDS) analysis. Linear analysis of the Pd nanoparticle region in the high-resolution

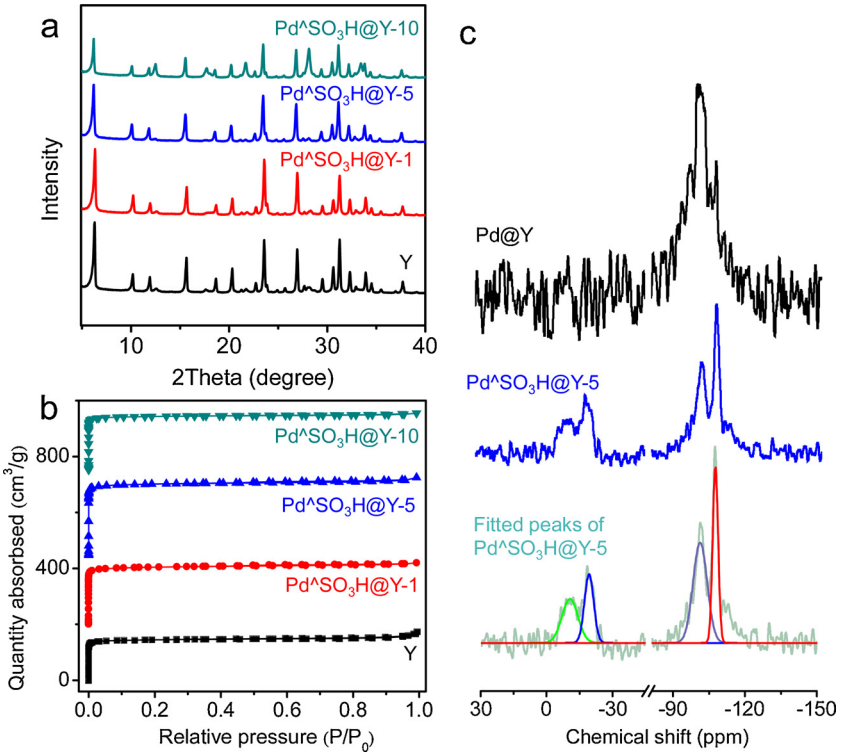

Fig. 1. (a) XRD, (b) N_2 sorption isotherms, and (c) ^{29}Si NMR spectra of various samples.

STEM image of Pd^SO_3H@Y-5 shows enriched S signal around the Pd nanoparticles (Fig. 2h). For example, the S/Pd ratio appears at ~0.3 in the central of Pd nanoparticle and increases to ~2.7 on the Pd surface region. Similar phenomenon is also observed on other randomly selected Pd nanoparticle (Figs. S10 and S11), confirming that the Pd nanoparticles are indeed surrounded by the S species, which forms geometrically closest metal nanoparticles with sulfonic acid groups, as presented in the scheme of Fig. 2g. EDS analysis in the SEM characterization shows obvious sulfur signal on the zeolite surface but undetectable Pd species, which might be due to that there are partial organosilane species uncoordinated with Pd on the external surface of the zeolite crystals (Fig. S12). In contrast, the conventional supported catalyst, such as Pd/Y-SO_3H, exhibits randomly distributed Pd and S species (Fig. S13).

It is worth mentioning that the unique synthesis route ensures the presence of metal-acid interfaces in the Pd^SO_3H@Y-5: (i) the -SH groups in the precursor strongly coordinate with Pd nanoparticles during the zeolite crystallization process, forming Pd-SH compound within the zeolite crystals on Pd^SH@Y sample; (ii) when the -SH is transformed into -SO_3H, the groups of -SO_3H are still close to Pd nanoparticles, as confirmed by the EDS analysis (Figs. 2f-h and S10), because the locations of Pd nanoparticles and organic groups were

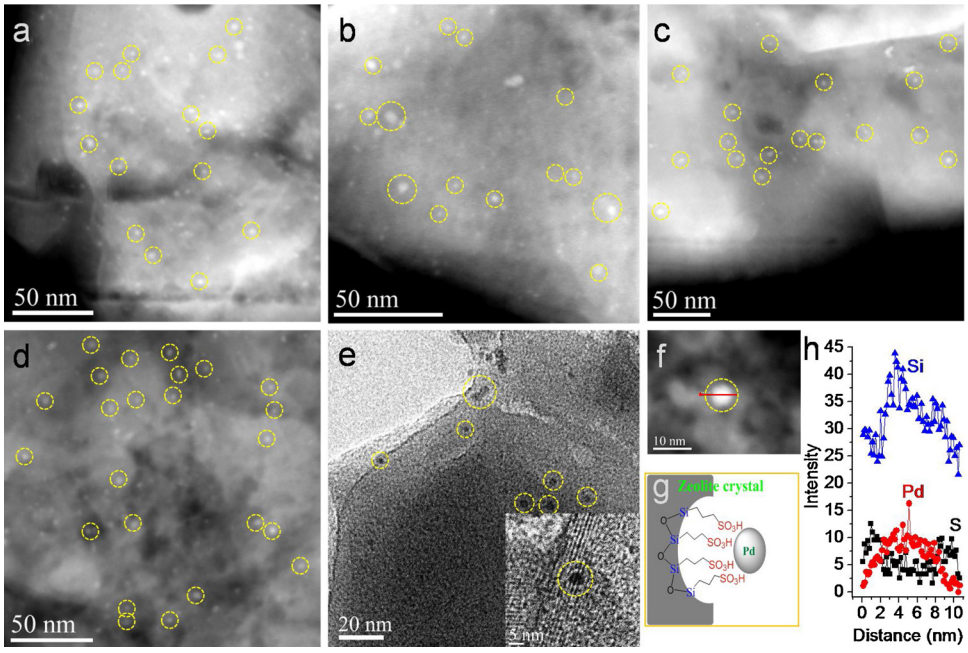

Fig. 2. Electronic microscopic characterization of Pd^SO_3H@Y samples. HAADF-STEM images of the (a) Pd^SO_3H@Y-1, (b) Pd^SO_3H@Y-5, and (c) Pd^SO_3H@Y-10 samples. Tomographic section (d) STEM and (e) TEM images of the Pd^SO_3H@Y-5 sample. (h) Linear EDS analysis of the Pd nanoparticle region in STEM image (f). (g) Model of Pd-acid interface within zeolite crystal. Inset in e, enlarge view of the Pd nanoparticle and zeolite lattice.

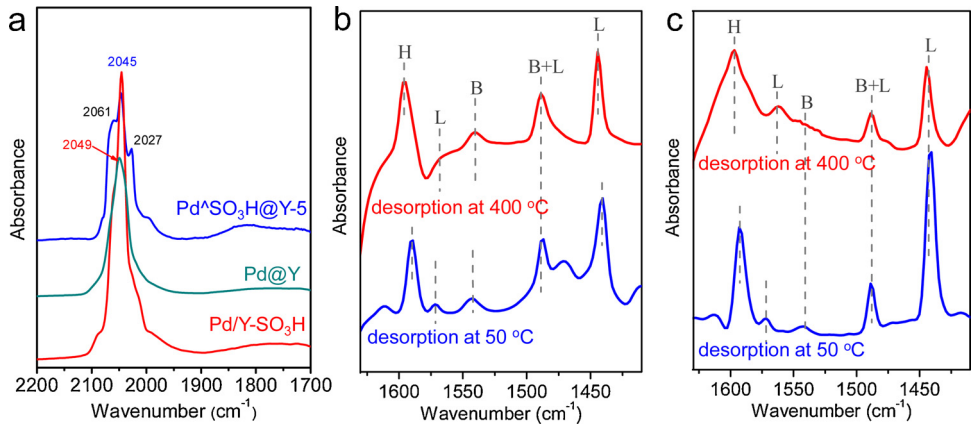

Fig. 3. (a) CO-adsorption FTIR spectra of the Pd^SO_3H@Y-5, Pd/Y-SO_3H, and Pd@Y. Pyridine-adsorption FTIR spectra of (b) Pd^SO_3H@Y-5 and (c) general Y zeolite after desorption at 50 and 400 °C.

Table 1
Data characterizing the performances of various catalysts in the HDO of furfural[a].

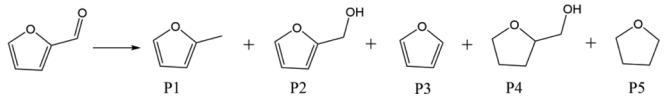

Entry	Catalyst	Conv. (%)	Product selectivity (%)						Balance (%)[b]
			P1	P2	P3	P4	P5	Others	
1	blank	2.4	–[c]	–	–	–	–	–	97.5
2	Pd/SiO_2	79.1	–	90.2	–	7.8	–	2.0	99.2
3	Pd/Al_2O_3	> 99.5	30.0	29.5	3.6	34.2	–	3.7	98.0
4	Pd/C	> 99.5	39.9	24.8	8.9	26.4	–	–	98.4
5[d]	Pd/PVP colloid	> 99.5	14.2	40.0	5.9	37.0	< 1.0	1.2	100.3
6[e]	Pd/PVP + H_2SO_4	> 99.5	57.0	–	9.6	3.7	< 1.0	29.3[f]	100.9
7	Pd@Y	94.7	47.5	22.2	25.1	–	–	5.2	96.8
8	Pd^SO_3H@Y-1	> 99.5	77.2	10.0	12.5	–	–	< 1.0	97.4
9	Pd^SO_3H@Y-5	> 99.5	99.3	–	< 1.0	–	–	–	99.2
10	Pd^SO_3H@Y-10	> 99.5	98.9	–	< 1.0	–	–	–	99.0
11[g]	Pd^SO_3H@Y-5	> 99.5	96.4	–	3.1	–	–	< 1.0	100.7
12[h]	Pd^SO_3H@Y-5	> 99.5	–	25.0	33.4	–	–	41.6[i]	95.8
13	Pd/Y-SO_3H	> 99.5	49.7	33.2	5.0	7.6	–	4.5	100.1

[a] Reaction conditions: 1.0 mmol of furfural, 40 mg of catalyst, 6 mL of methanol solvent, 1.0 MPa of H_2-Ar mixed gas (molar ratio of H_2/Ar at 1), 130 °C, 6 h.
[b] The molecule balance according to the amount of furan/tetrahydrofuran rings before and after the reactions.
[c] Undetectable.
[d] 1.6 mL of Pd colloid (Pd concentration at 0.2 g/L).
[e] 0.16 mL of Pd colloid and 5 mg of H_2SO_4 (70 wt% aqueous solution).
[f] Difurfuryl ether and some others.
[g] 6 mL of ethanol solvent.
[h] 6 mL cyclohexane solvent.
[i] Ethers and some others.

already immobilized by the rigid zeolite framework. This feature would benefit the formation of abundant metal-acid interfaces for maximizing the metal-acid synergism.

Fig. 3a shows CO-adsorption FTIR spectra of various samples. When CO is introduced to the solid samples, the Pd@Y and Pd/Y-SO_3H exhibits similar bands at 2045–2049 cm^{-1} assigned to the linearly bonded CO on metallic Pd sites [28–30]. In contrast, Pd^SO_3H@Y-5 shows additional bands at 2061 and 2027 cm^{-1}, assigning to CO bonded on the positively and negatively charged Pd sites, respectively. This phenomenon might be due to the formation of Pd-SO_3H interfaces, becasue the Pd favors to interact with protons in a confined environment to form Pd-proton adducts [28–30]. Considering the Pd^SO_3H@Y-5 and Pd/Y-SO_3H have the same Pd nanoparticles, Y zeolite, and -SO_3H species, the difference for CO adsorption is resulted from the contribution of Pd-SO_3H interfaces in the Pd^SO_3H@Y-5.

Furthermore, pulsed CO chemisorption measurement confirms partial blockage of Pd sites on Pd^SO_3H@Y-5 catalyst, giving the Pd dispersion at 23% that is remarkably lower than that of the supported catalyst with similar Pd nanoparticle diameters (39% over Pd/Y-SO_3H). This feature is well consistent with that of the zeolite encapsulated metal catalysts.

The acidity of Pd^SO_3H@Y catalyst is identified by pyridine-adsorption FTIR spectroscopy, which is a practical technique to characterize acidity in the solid acid catalysts. After adsorption of pyridine and desorption treatment at 50 °C, the Pd^SO_3H@Y-5 and Y zeolite give the peaks at 1445 and 1571 cm^{-1}, which are assigned to the coordinately bound pyridine on Lewis acid sites (Fig. 3b and c) [31–33]. The bands at 1540 cm^{-1} existing on both samples are assigned to the pyridine adsorbed on Brønsted acid sites, which might originate from the protons in zeolite micropores and/or sulfonic acid groups [31–33]. After desorption at 400 °C, the pyridine on Brønsted acid sites of Y zeolite are significantly reduced (see the reduced band at 1540 cm^{-1} in

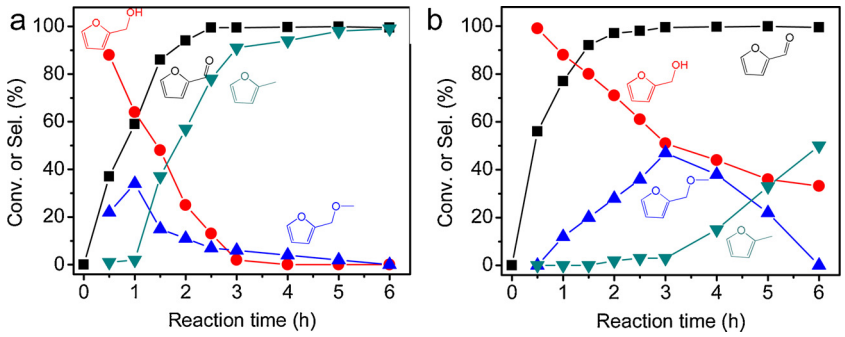

Fig. 4. Dependences furfural conversions and product selectivities in the HDO of furfural over (a) Pd^SO$_3$H@Y-5 and (b) Pd/Y-SO$_3$H catalysts. The reaction conditions are the same to those in Table 1.

Fig. 3c). In contrast, the pyridine molecules were still strongly adsorbed on the Pd^SO$_3$H@Y-5 after the equivalent desorption treatment (Fig. 3b), supporting the strong interaction between pyridine and the Brønsted acid sties of Pd^SO$_3$H@Y-5. Similar phenomenon was also observed in the Pd^SO$_3$H@Y-10 catalyst (Fig. S14), which should be reasonably attributed to the sulfonic acid groups with stronger acidity than the protons in zeolite framework.

Overall, the aforementioned characterizations demonstrate (1) successful fixation of Pd nanoparticles and sulfonic acid groups within the zeolite crystals, (2) the geometrically closest metal-acid distribution with bifunctional interfaces, (3) strong acidity of sulfonic acid groups, and (4) accessible active sites via the zeolite micropores. Such features realize a proof-of-concept design for the zeolite immobilized bifunctional catalysts, whose schematic presentation of the core-shell structure is illustrated in Scheme 1.

3.2. HDO of furfural

The catalytic evaluation of the samples starts from the HDO of furfural (Table 1), which is an important platform molecule in biomass conversion [34–38]. The furfural conversion proceeds complex pathways, and the methyl furan is regarded as a promising feedstock for fine chemical synthesis [38–43]. The HDO was carried out in a batch reactor with methanol solvent. The blank run without catalysts (entry 1) fails to obtain any products of methyl furan (P1), furfuryl alcohol (P2), furan (P3), tetrahydrofurfuryl alcohol (P4), and tetrahydrofuran (P5). The conventionally supported Pd catalyst such as Pd/SiO$_2$, is active for the reaction, giving furfural conversion at 79.1% with undetectable methyl furan (entry 2). The commercial Pd/Al$_2$O$_3$ and Pd/C catalysts, which are practically used in various reactions, give full conversion of furfural but sill poor selectivity for methyl furan (30.0 and 39.9%, entries 3 and 4). Even the soluble Pd colloid stabilized by PVP (Pd/PVP), a highly active catalyst for the hydrogenations, catalyzed the complete conversion of furfural but with methyl furan selectivity at only 14.2% (entry 5). In these cases, the furfuryl alcohol and tetrahydrofurfuryl alcohol always appear as dominant products. It is well-known that the acid sites benefit the HDO reaction, therefore, we performed the HDO of furfural over Pd/PVP catalyst with H$_2$SO$_4$ in the reaction liquor, showing remarkably enhanced methyl furan selectivity (57.0%, entry 6) compared with the acid-free reaction (14.2%, entry 5). The Pd@Y catalyst with both Pd nanoparticles and acidic sites in zeolite crystals shows the methyl furan selectivity at 47.5% and furfural conversion at 94.7% (entry 7), confirming the important role of acid sites for accelerating the HDO transformation.

Interestingly, the Pd^SO$_3$H@Y-1 shows full conversion of furfural with methyl furan selectivity at 77.2% (entry 8), and the Pd^SO$_3$H@Y-5 and -10 catalysts with more -SO$_3$H acid sites exhibit the methyl furan selectivities at 99.3 and 98.9%, respectively (entries 9 and 10). Such performances steadily outperform the conventional supported catalysts for selective furfural hydrogenation in literatures, although the Pd sites in the Pd^SO$_3$H@Y catalysts are less accessible. In contrast, the Pd/Y-SO$_3$H shows low methyl furan selectivity at 49.7% (entry 13). Considering these catalysts have similar Pd nanoparticles, sulfonic acid groups, and zeolite matrix, the difference in catalytic performances should be reasonably assigned to the location of acid sites and Pd nanoparticles in the catalysts.

The tetrahydrofurfuryl alcohol from the hydrogenation of furan ring was always produced over the conventional supported catalysts (e.g. Pd/SiO$_2$, Pd/Al$_2$O$_3$, Pd/C, and Pd/Y-SO$_3$H, Table 1), which is in good agreement with the phenomenon in the literature [35,44,45]. Interestingly, the products from C=C hydrogenation (tetrahydrofurfuryl alcohol and tetrahydrofuran) are almost undetectable over the zeolite fixed catalysts (Pd^SO$_3$H@Y and Pd@Y, Table 1), which might be explained by the zeolite fixed structure and/or organosilane groups controlling the steric adsorption of furfural molecules on the Pd surface to hinder the C=C hydrogenation [44].

3.3. Kinetic study

Take deep insight into the different catalytic performances of catalysts containing Pd and sulfonic acid group, we analyzed the intermediates during the HDO of furfural. Fig. 4a shows dependences of furfural conversions and selectivities of various products on time over the Pd^SO$_3$H@Y-5. The furfuryl alcohol, a primarily hydrogenated product, appears as a dominant product in the beginning of the reaction accompanied by the existence of methyl furfural ether (MFE). The maximized MFE selectivity occurs at 34.1% at 1 h with decreased furfuryl alcohol selectivity, while the reaction for longer time causes fast transformation of MFE into form methyl furan. As shown in the transformation pathways in Scheme 2, it is reasonably proposed that the furfural could be firstly hydrogenated into furfural alcohol over the Pd nanoparticle, which can react with methanol solvent to form MFE via dehydration on the acid sites. The MFE is further hydrogenolyzed on the Pd nanoparticles to produce methyl furan, which is a typical cascade reaction over the bifunctional sites. Notably, the reaction reach a steady state after 3 h over the Pd^SO$_3$H@Y-5 catalyst. After this process, the transformation of substrate (furfuran) and intermediate molecules (furfuryl alcohol and MFE) are slow down because of the low

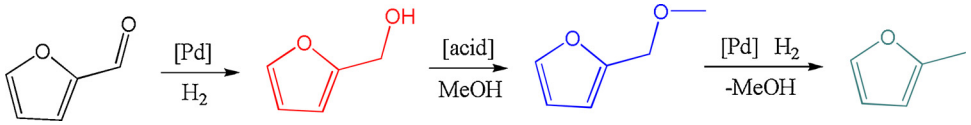

Scheme 2. The elementary reaction steps in the HDO of furfural to produce methyl furan.

Table 2
Reaction rates of Pd^SO$_3$H@Y-5 and Pd/Y-SO$_3$H catalysts in the elementary steps of furfural HDO[a].

Entry	Reactions	Reaction rate (mmol $g^{-1} h^{-1}$)[b]	
		Pd^SO$_3$H@Y-5	Pd/Y-SO$_3$H
1	Furfural hydrogenation	63.8	80.9
2[c]	Furfuryl alcohol and methanol etherification	9.2	11.7
3	MFE hydrogenation	19.9	27.3

[a] Reaction conditions: 130 °C, 1.0 M P of H_2-Ar mixed gas (molar ratio of H_2/Ar at 1), 50 mg of catalyst, 3 mmol of substrate, 10 ml of methanol.
[b] The reaction rates were calculated from the substrate conversion in the beginning of the reaction (5–20 min).
[c] 1.0 MPa of Ar was used without H_2.

concentration of these molecules in the reaction liquor rather than the catalyst deactivation. In this process, we conclude that the MFE act as a crucial intermediate for the selective HDO, because direct HDO of furfuryl alcohol by cleaving strong C—OH bond is energy-unfavorable. More evidence for this viewpoint is achieved by the test in furfural HDO in cyclohexane solvent (entry 12), which switched off the MFE route in a methanol-free liquor, giving almost undetectable methyl furan. When the Pd/Y-SO$_3$H catalyst was used, similar reaction trends with Pd^SO$_3$H@Y-5 are observed under the equivalent conditions, showing MFE as a dominant intermediate and then transforming into methyl furfural (Fig. 4b). Notably, the MFE selectivity is 11.8% at 1 h, lower than 34.1% over the Pd^SO$_3$H@Y-5 at the same reaction time, suggesting that the formation of MFE is relatively slow over Pd/Y-SO$_3$H. These data also explain faster production and transformation of MFE over the Pd^SO$_3$H@Y-5 than that over the Pd/Y-SO$_3$H.

Table 2 shows reaction rates of the Pd^SO$_3$H@Y-5 and Pd/Y-SO$_3$H catalysts in the elementary reactions of the furfural HDO, including hydrogenation of furfural into furfuryl alcohol, etherification of furfuryl alcohol with methanol to MFE, and hydrogenation of MFE into methyl furan. Clearly, the etherification of furfuryl alcohol with methanol to MFE acts as the rate-determining step for the overall reaction rate of the furfural HDO. However, the MEF formation rate over the Pd/Y-SO$_3$H is even slightly faster than that over Pd^SO$_3$H@Y-5 in the control step (etherification of furfuryl alcohol with methanol, 9.2 VS 11.7 mmol $g^{-1} h^{-1}$), because these catalysts have similar sulfonic acids but the acids on the Pd/Y-SO$_3$H catalyst are more accessible. Such observation is quite different from the general knowledge that higher product yield must originate from faster rate of control step.

Furthermore, we performed the production of methyl furan from different feedstocks including furfural, furfuryl alcohol, and MFE, and the productivities of methyl furan over the Pd^SO$_3$H@Y-5 and Pd/Y-SO$_3$H catalysts are presented in Table 3. Compared with Pd/Y-SO$_3$H, the Pd^SO$_3$H@Y-5 catalyst exhibits lower productivity of methyl furan from MFE (28.2 VS 35.1 mmol $g^{-1} h^{-1}$, Table 3). However, when furfural and furfuryl alcohol were used as feedstocks, the Pd^SO$_3$H@Y-5 shows significantly higher methyl furan productivities than the Pd/Y-SO$_3$H catalyst (Table 3).

On the basis of these results, it is suggested that the Pd^SO$_3$H@Y-5 is

Table 3
Productivities of methyl furan from the HDO of various feeds over Pd^SO$_3$H@Y-5 and Pd/Y-SO$_3$H catalysts[a].

Feed	Catalyst	Methyl furan productivity (mmol $g^{-1} h^{-1}$)[b]
Furfural	Pd^SO$_3$H@Y-5	18.6
	Pd/Y-SO$_3$H	12.9
Furfuryl alcohol	Pd^SO$_3$H@Y-5	18.2
	Pd/Y-SO$_3$H	14.5
MFE	Pd^SO$_3$H@Y-5	28.2
	Pd/Y-SO$_3$H	35.1

[a] Reaction conditions: 130 °C, 1.0 M P of H_2-Ar mixed gas (molar ratio of H_2/Ar at 1), 50 mg of catalyst, 3 mmol of substrate, 10 ml of methanol.
[b] The productivities were calculated in the beginning of the reaction (50–60 min).

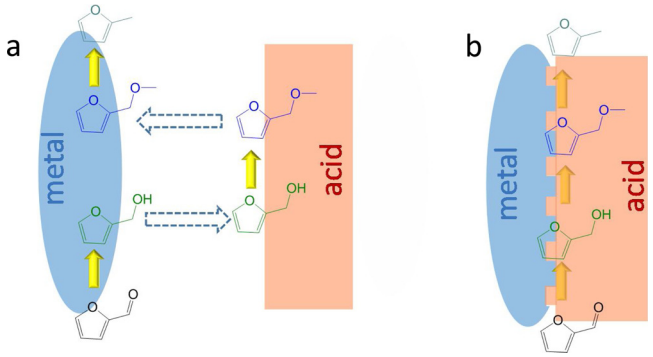

Scheme 3. Scheme showing the reaction pathways over (a) geometrically separated metal-acid sites and (b) synergistic metal-acid interfaces. The yellows arrows highlight the hydrogenation/etherification elementary steps. The dotted arrows in (a) highlight the repeated diffusion of intermediate molecules between the geometrically separated metal-acid sites.

invalid to enhance the rate-control steps in the HDO, but it remarkably strengthens the integrated reaction process containing cascade elementary steps. This feature is reasonable owing to the Pd-acid interfaces within the zeolite crystals, where the intermediates formed on the metal (acid) sites could be immediately transformed on the nearby acid (metal) sites. This process could avoid the molecular diffusion between the multiple active sites, which efficiently accelerates the whole reaction process (Scheme 3b). In contrast, the intermediate molecules have to diffuse repeatedly between the geometrically separated metal-acid sites on the conventionally supported catalysts (Scheme 3a), leading to relatively low efficacy in the cascade catalysis.

3.4. Catalyst recyclability

The recyclabilities are crucial for the potential industrial applications. Very importantly, the Pd^SO$_3$H@Y-5 exhibits stable performances in the recycling tests in HDO of furfural (Fig. S15a). Even in the 13th run, the catalyst still shows constant furfural conversion and methyl furan selectivity, which are completely comparable to those on the fresh catalyst. Fig. S15b and S15c give the dependences of furfural conversion and furan selectivity on time over Pd^SO$_3$H@Y-5 catalyst in the 1st, 5th, and 13th runs, respectively. The curves in these runs are almost the same attributing to the unchanged performances, which further confirms the excellent recyclability of Pd^SO$_3$H@Y-5 catalyst. The sulfur elemental analysis and ICP-OES measurements demonstrate that the Pd and S leaching are negligible on the catalyst. Fig. S16 shows the XRD pattern, N_2 adsorption-desorption isotherms, and SEM image of the Pd^SO$_3$H@Y-5 sample after the 13th run in the HDO of furfural, which give typical peaks of FAU structure with good crystallinity, high surface area at 593.2 m^2/g, and unchanged morphology compared with the fresh catalyst, respectively. The EDS analysis of the used Pd^SO$_3$H@Y-5 after 13th run still gives clear signals around the Pd nanoparticles (Fig. S17), confirming the stable Pd-acid interfaces. In contrast, the Pd/Y-SO$_3$H catalyst showed a reduced furan selectivity in the 6th run (Fig. S18), which might be due to the Pd leaching during the recycle tests (Pd

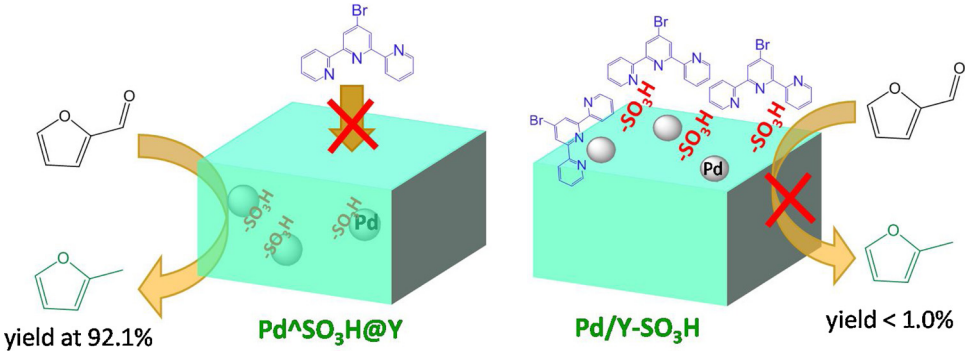

Scheme 4. Scheme showing the HDO of furfural over Pd^SO_3H@Y and Pd/Y-SO_3H catalysts with the existence of BTP. Reaction conditions: 1.0 mmol of furfural, 30 mg of catalyst, 6 mL of methanol solvent, 0.4 mmol of BTP, 1.0 MPa of H_2-Ar mixed gas (molar ratio of H_2/Ar at 1), 130 °C, 8 h.

leaching at ~6% by ICP analysis).

3.5. HDO of phenolic molecule

It is interesting to note that the concept on zeolite-enveloped metal-acid interface catalysts is not only limited to the HDO of furfural, but also can be applied in the upgrading of other biomass-derived oxygenates (Fig. S19). For example, in the HDO of model compounds including phenol and cresol in biomass pyrolysis oil, which are typical cascade reactions involving multiple metal- and acid-catalyzed individual reactions [20,21], the Pd^SO_3H@Y-5 also has high cyclohexane and methylcyclohexane yields (> 99.0%). These values are remarkably higher than those over the Pd/Y-SO_3H catalysts (yields at 87% for cyclohexane and 65% for methylcyclohexane), demonstrating the expansibility of the zeolite enveloped metal-acid catalysts for the biomass conversion.

3.6. Shape-selective catalysis

Meanwhile, it is worth noting that the zeolite matrix with micropores might provide an opportunity for shape-selective catalysis, which is an important advantage for the heterogeneous catalysis [46–49]. Following this hypothesis, we performed the HDO of furfural with the existence of 4″-bromo-2,2′:6′,2″-terpyridine (BTP, Scheme S1), which is known to poison the Pd and acid sites. As presented in Scheme 4, the Pd^SO_3H@Y-5 still shows the methyl furan yield at 92.1%, demonstrating the catalytic activity of Pd-acid interface sites are well maintained even in the presence of BTP. This phenomenon is in accordance with the shape-selective function where the zeolite sheath hindered the diffusion of bulky BTP molecule to the Pd-acid sites. In contrast, the Pd/Y-SO_3H is completely inactive for the HDO of furfural with undetectable methyl furan under the equivalent conditions, because the groups in BTP easily poison the Pd and acid sites on the catalyst.

4. Conclusions

In summary, we have demonstrated the construction of metal-acid bifunctional active sites within the zeolite crystals to form a core-shell catalyst. The Pd nanoparticles and sulfonic acid groups enveloped within zeolite crystals exhibit significantly improved properties in the catalytic HDO of biomass-derived oxygenates, such as HDO of furfural into valuable methyl furan. The current synthetic methods by zeolite enveloption offer a new avenue for enhancing the synergism between multiple active sites, providing a promising approach to strengthen the cascade catalysis.

Acknowledgments

This work was supported by the National Key Research and Development Program of China (2018YFD1000806-01), the National Natural Science Foundation of China (21822203, 91645105, and 91634201), and the Natural Science Foundation of Zhejiang Province (LR18B030002).

Appendix A. Supplementary data

Supplementary material related to this article can be found, in the online version, at doi:https://doi.org/10.1016/j.apcatb.2019.05.022.

References

[1] F. Jiao, J. Li, X. Pan, J. Xiao, H. Li, H. Ma, M. Wei, Y. Pan, Z. Zhou, M. Li, S. Miao, J. Li, Y. Zhu, D. Xiao, T. He, J. Yang, F. Qi, Q. Fu, X. Bao, Science 351 (2006) 1065–1068.
[2] G.W. Huber, J.N. Chheda, C.J. Barrett, J.A. Dumesic, Science 308 (2005) 1446–1450.
[3] J.N. Chheda, G.W. Huber, J.A. Dumesic, Angew. Chem. Int. Ed. 46 (2007) 7164–7183.
[4] Z. Lin, W. Wan, S. Yao, J.G. Chen, Appl. Catal. B-Environ. 233 (2018) 160–166.
[5] Q.-N. Xia, Q. Cuan, X.-H. Liu, X.-Q. Gong, G.-Z. Lu, Y.-Q. Wang, Angew. Chem. Int. Ed. 53 (2014) 9755–9760.
[6] K.A. Resende, A.H. Braga, F.B. Noronha, C.E. Hori, Appl. Catal. B-Environ. 245 (2019) 100–113.
[7] T.C. Lanzac, R. Palos, I. Hita, J.M. Arandes, J.R. Mirasol, T. Cordero, J. Bilbao, P. Castaño, Appl. Catal. B-Environ. 239 (2018) 513–524.
[8] C.S. Shalaby, S.K. Saha, X. Ma, C. Song, Appl. Catal. B-Environ. 101 (2011) 718–726.
[9] E. Ochoa, D. Torres, R. Moreira, J.L. Pinilla, I. Suelves, Appl. Catal. B-Environ. 239 (2018) 463–474.
[10] E. Furimsky, Appl. Catal. A-Gen. 199 (2000) 147–190.
[11] S. Crossley, J. Faria, M. Shen, D.E. Resasco, Science 327 (2010) 68–72.
[12] G.W. Huber, P. O'Connor, A. Corma, Appl. Catal. A-Gen. 329 (2007) 120–129.
[13] G.-H. Wang, Z. Cao, D. Gu, N. Pfänder, Angew. Chem. Int. Ed. 55 (2016) 8850–8855.
[14] J. He, T. Xu, Z. Wang, Q. Zhang, W. Deng, Y. Wang, Angew. Chem. Int. Ed. 51 (2012) 2438–2442.
[15] C. Zhao, J.A. Lercher, Angew. Chem. Int. Ed. 51 (2012) 5935–5940.
[16] L.T. Mika, E. Cséfalvay, A. Németh, Chem. Rev. 118 (2018) 505–613.
[17] R.W. Gosselink, D.R. Stellwagn, J.H. Bitter, Angew. Chem. Int. Ed. 52 (2013) 5089–5092.
[18] C. Li, X. Zhao, A. Wang, G.W. Huber, T. Zhang, Chem. Rev. 115 (2015) 11559–11624.
[19] K.L. Luska, P. Migowski, S.E. Sayed, W. Leiner, Angew. Chem. Int. Ed. 54 (2015) 15750–15755.
[20] P. Ferrini, R. Rinaldi, Angew. Chem. Int. Ed. 53 (2014) 8634–8639.
[21] M. Mascal, S. Dutta, I. Gandarias, Angew. Chem. Int. Ed. 53 (2014) 1854–1857.
[22] E. Kordouli, B. Pawelec, C. Kordulis, A. Lycourghiotis, J.L.G. Fierro, Appl. Catal. B-Environ. 238 (2018) 147–160.
[23] J. Chen, J. Huang, L. Chen, L. Ma, T. Wang, U.I. Zakai, ChemCatChem 5 (2013) 1598–1605.
[24] N. Yan, Y. Yuan, R. Dykeman, Y. Kou, P.J. Dyson, Angew. Chem. Int. Ed. 49 (2010) 5549–5553.
[25] C.A. Teles, P.M. de Souza, A.H. Braga, R.C.R. Neto, A. Teran, G. Jacobs, D.E. Resasco, F.B. Noronha, Appl. Catal. B-Environ. 249 (2019) 292–305.
[26] J. Zhang, L.D. Ellis, B. Wang, M.J. Dzara, C. Sievers, S. Pylypenko, E. Nikolla, J.W. Medlin, Nat. Catal. 1 (2018) 148–155.
[27] J. Zhu, L. Wang, Q. Hu, L. Zhang, S. Xu, X. Dong, X. Gao, R. Ma, X. Meng, F.-S. Xiao, ACS Catal. 8 (2008) 5250–5254.
[28] W.M.H. Sachtler, Metal clusters in zeolites: an intriguing class of catalysts, Acc. Chem. Res. 26 (1993) 383–387.

[29] L.L. Sheu, H. Knoezinger, W.M.J. Sachtler, J. Am. Chem. Soc. 111 (1989) 8125–8131.
[30] Z. Zhang, T.T. Wong, W.M.H. Sachtler, J. Catal. 128 (1991) 13–22.
[31] A.A. Marianou, C.M. Michailof, A. Pineda, E.F. Iloopoulou, K.S. Triantafyllidis, A.A. Lappas, Appl. Catal. A-Gen. 555 (2018) 75–87.
[32] W. Xu, T. Ollevier, F. Kleitz, ACS Catal. 8 (2018) 1932–1944.
[33] N. Musselwhite, K. Na, K. Sabyrov, S. Aayogu, G.A. Somorjai, J. Am. Soc. Chem. 137 (2015) 10231–10237.
[34] P. Claus, Top. Catal. 5 (1998) 51–62.
[35] H. Zhang, X.-K. Gu, C. Canlas, A.J. Kropf, P. Aich, J.P. Greeley, J.W. Elam, R.J. Meyers, J.A. Dumesic, P.C. Stair, C.L. Marshall, Angew. Chem. Int. Ed. 53 (2014) 12132–12136.
[36] N.M. Briggs, L. Barrett, E.C. Wegener, L.V. Herrera, L.A. Gomez, J.T. Miller, S.P. Crossley, Nat. Commun. 9 (2018) 3827–3833.
[37] E.I. Gürbüz, J.M.R. Gallo, D.M. Alonso, S.G. Wettstein, W.Y. Lim, J.A. Dumesic, Angew. Chem. Int. Ed. 52 (2013) 1270–1274.
[38] L. Bui, H. Luo, W.R. Gunther, Y.R. Leshkov, Angew. Chem. Int. Ed. 52 (2013) 8022–8025.
[39] B.J. O'Neill, D.H.K. Jackson, A.J. Crisci, C.A. Farberow, F. Shi, A.C.A. Rubio, J. Lu, P.J. Dietrich, X. Gu, C.L. Marshall, P.C. Stair, J.W. Elam, J.T. Miller, F.H. Ribeiro, P.M. Voyles, J. Greeley, M. Mavrikakis, S.L. Scott, T.F. Kuech, J.A. Dumesic, Angew. Chem. Int. Ed. 52 (2013) 13808–13812.
[40] J.G. Stevens, R.A. Bourne, M.V. Twigg, M. Poliakoff, Angew. Chem. Int. Ed. 49 (2010) 8856–8859.
[41] J. Zhang, B. Wang, E. Nikolla, J.W. Medin, Angew. Chem. Int. Ed. 56 (2017) 6594–6598.
[42] I. Scodeller, S. Mansouri, D. Morvan, E. Muller, K.O. Vigier, R. Wischert, F. Jérôme, Angew. Chem. Int. Ed. 57 (2018) 10510–10514.
[43] Y. Deng, R. Gao, L. Lin, T. Liu, X.-D. Wen, S. Wang, D. Ma, J. Am. Chem. Soc. 140 (2018) 14481–14489.
[44] S.H. Pang, C.A. Schoenbaum, D.K. Schwartz, J.W. Medlin, Nat. Commun. 4 (2013) 2448.
[45] Y. Nakagawa, K. Takada, M. Tamura, K. Tomishige, ACS Catal. 4 (2014) 2718–2726.
[46] L. Wang, G. Wang, J. Zhang, C. Bian, X. Meng, F.-S. Xiao, Nat. Commum. 8 (2017) 15240–15247.
[47] T.-L. Cui, W.-Y. Ke, W.-B. Zhang, H.-H. Wang, X.-H. Li, J.-S. Chen, Angew. Chem. Int. Ed. 55 (2016) 9178–9182.
[48] S. Goel, S.I. Zones, E. Iglesia, J. Am. Chem. Soc. 136 (2014) 15280–15290.
[49] L. Liu, U. Díaz, R. Arenal, G. Agostini, P. Concepción, A. Corma, Nat. Mater. 16 (2017) 132–138.